

Pulsed power to control growth of silicon nanoparticles in low temperature flowing plasmas



Cite as: J. Appl. Phys. **132**, 073301 (2022); doi: [10.1063/5.0100380](https://doi.org/10.1063/5.0100380)

Submitted: 24 May 2022 · Accepted: 1 July 2022 ·

Published Online: 15 August 2022



View Online



Export Citation



CrossMark

Steven J. Lanham,^{1,a)} Jordyn Polito,^{1,b)} Zichang Xiong,^{2,c)} Uwe R. Kortshagen,^{2,d)} and Mark J. Kushner^{1,3,e)}

AFFILIATIONS

¹Department of Chemical Engineering, University of Michigan, 1301 Beal Ave., Ann Arbor, Michigan 48109-2122, USA

²Department of Mechanical Engineering, University of Minnesota, 111 Church Street SE, Minneapolis, Minnesota 55455, USA

³Department of Electrical Engineering and Computer Science, University of Michigan, 1301 Beal Ave., Ann Arbor, Michigan 48109-2122, USA

^{a)}sjlanham@umich.edu

^{b)}jopolito@umich.edu

^{c)}xion1832@umn.edu

^{d)}korts001@umn.edu

^{e)}Author to whom correspondence should be addressed: mjkush@umich.edu

ABSTRACT

Low-temperature plasmas have seen increasing use for synthesizing high-quality, mono-disperse nanoparticles (NPs). Recent work has highlighted that an important process in NP growth in plasmas is particle trapping—small, negatively charged nanoparticles become trapped by the positive electrostatic potential in the plasma, even if only momentarily charged. In this article, results are discussed from a computational investigation into how pulsing the power applied to an inductively coupled plasma (ICP) reactor may be used for controlling the size of NPs synthesized in the plasma. The model system is an ICP at 1 Torr to grow silicon NPs from an Ar/SiH₄ gas mixture. This system was simulated using a two-dimensional plasma hydrodynamics model coupled to a three-dimensional kinetic NP growth and trajectory tracking model. The effects of pulse frequency and pulse duty cycle are discussed. We identified separate regimes of pulsing where particles become trapped for one pulsed cycle, a few cycles, and many cycles—each having noticeable effects on particle size distributions. For the same average power, pulsing can produce a stronger trapping potential for particles when compared to continuous wave power, potentially increasing particle mono-dispersity. Pulsing may also offer a larger degree of control over particle size for the same average power. Experimental confirmation of predicted trends is discussed.

Published under an exclusive license by AIP Publishing. <https://doi.org/10.1063/5.0100380>

I. INTRODUCTION

Plasma-based synthesis of nanometer-sized particles is an active area of research, showing desirable improvements over conventional methods of synthesizing nanoparticles (NPs).^{1–3} Plasma-based methods often require considerable tuning of the plasma source and operating conditions to produce NPs with desired properties (e.g., size distribution, particle crystallinity, and composition).^{3–5} These plasma sources are highly coupled systems, with small changes in operating conditions having outcomes on NP properties that are sometimes difficult to predict *a priori*. NPs having increased complexity (e.g., core-shell nanoparticles, where

composition varies spatially) are highly sought after for their tunable optical properties and require a greater degree of control of plasma properties to produce.^{6–10} Current plasma-based NP synthesis techniques will likely be challenged to keep up with the desired designs of NPs for optical and energy applications. Additional control techniques and understanding are needed for plasma-synthesis techniques to meet these demands. The plasmas of interest are flowing systems having pressures of up to a few Torr, typically a rare gas with a small fraction of the feedstock gases (e.g., SiH₄ for synthesizing Si NPs). Power is coupled to the plasma using inductive and capacitive excitation.

Pulsing the power applied to the plasma is a technique used in the plasma material processing community to control ion energies and fluxes to surfaces, particularly for microelectronics fabrication.^{11–16} Using a combination of source (plasma producing) and bias (voltage to accelerate ions) pulsing^{17,18} can improve processing capabilities over continuous wave power, enabling new fabrication techniques such as atomic layer etching.¹⁹ The concept of controlling ion energies to surfaces with pulsing is straight forward—positive ions are accelerated across the sheath in contact with the surface and strike the surface with an energy proportional to the sheath potential (for a collisionless sheath). For these conditions, control of ion fluxes is delegated to the control of the sheath potential. In practice, there are many complicating factors, such as collisions in the sheath, ion transit time compared to applied frequency, changes in dc bias voltage, spatial variation in the surface flux, and changes to plasma chemistry. In spite of these complications, pulsing the power is a flexible way to control the potential and charged species densities in the plasma. An extension of this concept could be applied to plasmas for NP synthesis to control their properties.

Pulsed power has been computationally investigated as a method for controlled growth of films from Si nanoparticles²⁰ and investigated experimentally.^{21,22} Power modulation (sometimes coupled with a modulated inflow of feedstock) has also been investigated for particle growth^{23,24} and has shown improvements in Si/SiO_x composite NPs for lithium-ion batteries.²⁵

Particles in low-temperature plasmas generally charge negative as a consequence of a higher electron temperature and mobility compared to ions. As a consequence of their negative charging, they are often confined in the plasma by the positive plasma potential and outwardly directed electric fields in the bounding sheaths to the plasma. There have been many studies leveraging negative particle charging to study fundamental physics, such as Yukawa interactions,²⁶ phase transitions, and more recently dynamic charging in the afterglow of plasmas.^{27–32} However, the charge of particles in the plasma varies greatly with size. In studies of transport processes and thermodynamics, micrometer-sized particles are typically used which acquire thousands of charges, and those charge states tend to be fairly stable. Smaller nanometer-sized particles may be a mix of negative, neutral, and in some cases positive particles, with an individual NP stochastically changing its charge state over time.^{33–35} In spite of NPs dynamically changing their charge, electrostatic trapping of nanometer-sized particles can occur even if particles are only temporarily charged negative, a condition that may enable particle growth and monodispersity.³⁶

In this article, we report on results from a computational investigation using pulsed power for nanoparticle synthesis in flowing low-temperature plasmas (LTPs). Simulations were performed of a cylindrical inductively coupled plasma (ICP) reactor sustained in a rare gas with a dilute silane precursor for various pulsed duty cycles and pulse repetition frequencies with other parameters held constant (2 cm reactor diameter, 50 SCCM of Ar/SiH₄ = 98/2, 1 Torr, and 10 W average). The computational platforms used in the study are a two-dimensional hybrid-multi-fluid plasma model coupled with a three-dimensional kinetic model for particle growth and trajectory tracking. The intent of this work is to assess how trapping of negatively and transiently charged

particles in the positive plasma potential influences growth rates and particle size distributions under various pulsed conditions compared to continuous wave (CW) power. (The trapping potential itself varies over the pulsed cycle.) We found that pulsing may offer increased control over particle size distributions. In particular, pulsing may be a method to increase particle monodispersity compared to continuous wave power under certain conditions. This narrowing of the size distribution is primarily due to increased trapping potential and negative particle charging when using pulsing with the same average power as CW plasmas. Particle sizes can also be tuned with the pulsing frequency and duty cycle by several factors over continuous power conditions.

The models used in this investigation are described in Sec. II. The effects of pulsing, considering duty cycle and pulse repetition frequency, on nanoparticle growth and trapping are discussed in Sec. III. Experimental confirmation of predicted trends is discussed in Sec. IV. Concluding remarks are in Sec. V.

II. DESCRIPTION OF THE MODELS

The plasma chemistry, growth, and transport of nanoparticles in LTPs involve complex multi-scale processes, which we address by using two separate but coupled models. The Hybrid Plasma Equipment Model (HPEM), a two-dimensional plasma multi-fluid hydrodynamics model (discussed in Sec. II A), was used to model the reactor scale plasma and obtain parameters needed to address the nanoparticle growth. The Dust Transport Simulator (DTS) is a three-dimensional kinetic model that was used to compute trajectories and growth of nanoparticles in the plasma and will be discussed in Sec. II B. Information is transferred between the two models to generate a self-consistent solution.

A. Reactor scale plasma model

The reactor-scale plasma chemistry and hydrodynamics were modeled using the Hybrid Plasma Equipment Model (HPEM), a two-dimensional multi-fluid plasma simulator, described in detail in Ref. 37. Briefly, the HPEM separates relevant physics into different modules, and information between modules is shared using time-slicing techniques. In this work, the Electromagnetics Module (EMM) was used to solve for azimuthal electric fields produced by an antenna powered at radio frequency (RF) and their absorption by the plasma. The EMM uses a frequency domain solution. Secondary electron emission from surfaces is addressed in the Electron Energy Transport Module (EETM), where a Monte Carlo technique is used to generate electron impact source functions. The Fluid Kinetics Poisson Module (FKPM) is the main time-stepping module and was used to compute separate fluid continuity, momentum, and temperature equations for each heavy species (neutrals and ions). Continuity and temperature equations are solved for electrons assuming a drift-diffusion formulation for momentum. Poisson's equation for the electric potential is solved semi-implicitly with each time step in the FKPM for self-consistency.

Rate coefficients for electron impact processes and electron transport coefficients are obtained from the electron energy distribution (EED) produced using a two-term spherical harmonic solution to Boltzmann's equation, assuming spatially averaged

composition weighted by electron density. EEDs are produced over a range of E/N (electric field/gas number density) producing a table that is interpolated as a function of electron temperature.

The Ar/SiH_4 reaction mechanism used in this work is an updated version of that used most recently in Lanham *et al.*,³⁸ with data from previous works.^{39–41} The mechanism has been expanded to include ArH^+ and H_3^+ , which have previously been found to be the dominant ions for silane plasmas under certain conditions.^{42,43} The species included in the simulation are listed in Table I.

Particle growth is addressed in the DTS that feeds back local values of NP density and charges to the FKPM. These values are then used in the charge balance for solution to Poisson's equation, for the attachment (or neutralization) of electrons and ions on the NPs.

B. DTS and nanoparticle growth model

NP transport and growth were addressed using a three-dimensional kinetic model, the DTS, embedded in the HPEM. The implementation used in this work has been described previously,³⁸ and so the physics and mechanics of the model will only be described briefly here. The DTS obtains plasma properties from the HPEM, including electric fields, and species densities, temperatures, and momentum flux fields. The precursors to NPs are randomly distributed between axial locations of 1.5–2.5 cm (between the left-most two coils in Fig. 1) with an initial radius of 0.5 nm and with no charge. The particle mass, charge, and positions are then integrated in time. Forces on particles are computed, divided by the mass to obtain acceleration, with trajectories being integrated using a second-order technique. Particle charge is integrated from currents derived using Orbital Motion Limited (OML) trajectories,^{44,45} considering individual contributions from electrons, positive ions, and negative ions. Small NPs (i.e., <10 nm) can have significant stochastic charging,⁴⁶ and so the integrated currents (discrete charge per time step) were treated as rare events with a Poisson distribution to emulate this effect and to maintain increments in charge as integer values.

The relevant forces acting on the particles include gravitational, electrostatic, and inter-particle Coulomb forces; ion drag; viscous fluid drag; thermophoresis; and Brownian motion. The gravitational force acting on nm size particles is small compared to other forces but was included for self-consistency. The electrostatic force is computed by charged particles' acceleration in the local

electric field. For negative charged particles, as is typical for the types of dusty plasmas considered in this work, the accelerating electric field points away from the peak in the plasma potential, which traps negative particles, while positive particles are accelerated out of the plasma. To account for the electrostatic forces between NPs, particles interact directly with each other through a shielded Coulombic force given by a spherically symmetric solution to the Debye Hückel equation.⁴⁷ Direct computation of all coulomb interactions between particles has poor scaling of order N^2 , so only particle interactions within a few linearized Debye lengths are

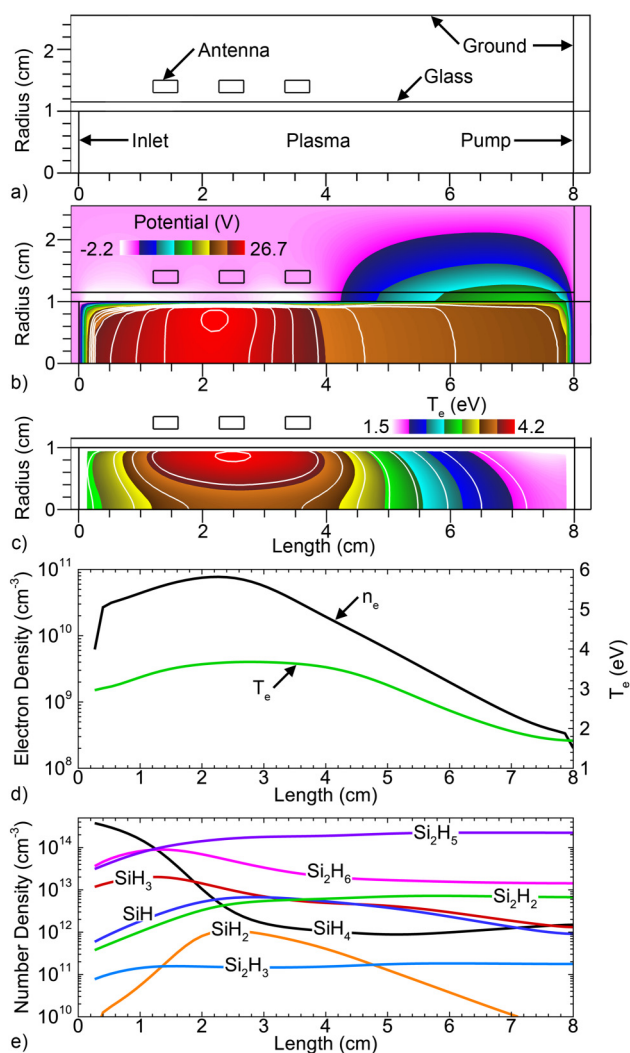


FIG. 1. Reactor and plasma properties for continuous wave power (1 Torr, 10 W power, 50 SCCM, $\text{Ar}/\text{SiH}_4 = 98/2$). (a) Schematic of the glass tube reactor, (b) electric potential in the plasma, (c) electron temperature, (d) electron density and temperature along the axis, and (e) Si nanoparticle growth precursor densities along the axis.

TABLE I. Species used in the plasma chemistry mechanism in the hybrid plasma equipment model.

Argon and electrons

Ar , $\text{Ar}(4s[3/2]_2^3P_2)$, $\text{Ar}(4s[3/2]_1^3P_1)$, $\text{Ar}(4s'[1/2]_0^3P_0)$,
 $\text{Ar}(4s'[1/2]_1^3P_1)$, $\text{Ar}(4p)$, $\text{Ar}(4d)$, Ar_2^* , Ar^+ , Ar_2^+ , e

Hydrogen species

H_2 , H_2^* , H , H^* , H^{**} , H^+ , H_2^+ , H_3^+ , ArH^+

Silane species

SiH_4 , SiH_3 , SiH_2 , SiH , Si_2H_6 , Si_2H_5 , Si_2H_3 , Si_2H_2 , SiH_3^+ ,
 SiH_3^- , SiH_2^- , Si_2H_5^-

calculated. This assumption has been found to be accurate in previous works due to the exponential decay in screening with distance.⁴⁸

The ion-drag force results from ions having a directed velocity approaching, for example, a negatively charged NP and undergoing a parabolic (positive ion) or hyperbolic (negative ion) orbit about the NP. The change in momentum of the ion due to this orbital motion is imparted to the NP. Since the momenta of positive ions are typically directed toward the boundaries of the plasma, the ion-drag force usually accelerates negative NPs toward the boundaries of the plasma. The ion-dust momentum transfer cross section is approximated using a semi-analytic expression from the work of Kilgore *et al.*⁴⁹ and coupled with the work of Khrapak *et al.*,⁵⁰ which agree well with simulation and modeling results.^{49,51}

The forces due to viscous fluid drag are derived for hard sphere particles from classical thermodynamics.^{52–54} The driving force for viscous fluid drag is to minimize the difference between the dust particle velocity and the bulk advective fluid velocity. The thermophoretic force can be an important force for particle motion, driven by temperature gradients, where particles move toward colder gas temperatures or surfaces. An effective force of Brownian motion due to random collisions with the background gas was also included. This force is more important for smaller particles, ~ 1 nm where the momentum transfer from individual atoms and molecules can be significant, while decreasing in significance with increasing particle size.

Growth of particles in the plasma was assumed to be dominated by the thermal flux of radicals to the particle surface. The time rate of change of mass of NP i is

$$\frac{dM_i}{dt} = \sum_j v_j N_j 4\pi r_i^2 S_{c,j} \Delta m_j, \quad v_j = \sqrt{\frac{8k_B T_j}{\pi m_j}}, \quad (1)$$

where the mass of dust particle i is M_i having radius r_i . The summation is over all particle growth species j , having thermal speed v_j , number density N_j , mass m_j , and temperature T_j . The quantity Δm_j is the mass added to the dust particle in each collision. The probability of specific species j sticking to the dust particle after a collision is $S_{c,j}$, and the values used in this work are shown in Table II.^{38,55} Particles are initialized in the plasma above a critical size in the regime where surface growth dominates, in this work assumed to be 1 nm. The mass and diameter of each dust pseudo-

TABLE II. Sticking coefficients (S_c) for species impacting Si NPs used to model NP growth.

Species	S_c
SiH ₄	0
SiH ₃	0.125
SiH ₂	0.66
SiH	0.945
Si ₂ H ₆	0
Si ₂ H ₅	0.1
Si ₂ H ₃	0.3
Si ₂ H ₂	0.66

particle are individually tracked to allow for there to be spatial dependence in particle growth processes. Particle agglomeration, as seen experimentally as chains of smaller spherical NPs, can be important under select conditions. Agglomeration is modeled by particles combining into a single larger spherical particle if they touch. However, for our conditions, this is rare as dust particles are typically charged negatively and do not gain enough kinetic energy to overcome Coulomb repulsion.

The conditions and timescales to grow nanoparticles in low-temperature plasmas are numerically difficult to resolve. A time slicing technique was employed to address these different timescales. First, the plasma is fully simulated under continuous wave power for several gas residence times with numerical acceleration to achieve steady-state species densities and temperature. Second, power to the plasma is then pulsed over several cycles to reach a periodic steady-state in the potential and charged species densities. The time averaged power during pulsing is the same as that for the CW power portion of the simulation. The gas residence times for growing NPs is typically on the order of ms and resolving multiple pulses at those frequencies would be impractical. Shorter pulses (50 μ s) were modeled in the plasma, which has the added benefit of having a negligible effect on long-term chemistry as the plasma achieves a steady state during the power-on period. Third, after a periodic steady-state for the plasma in pulsing is reached, particles are initialized in the DTS and time-slicing is used to scale the 50 μ s plasma pulse to longer times for the particles. The particles are tracked until they flow out of the reactor, which is designated by passing through a plane approximately 1 cm above the pump port where statistics are collected.

III. PULSED POWER FOR NP GROWTH

A. Pulsed vs CW power comparison

This work focuses on the methods that pulsed power may be used to control the growth of nanoparticles in flowing low-temperature plasma reactors. The rationale for this work is that NPs can be electrostatically trapped in flowing LTPs,^{6,8,9,56} and power modulation affects the trapping process. The charge on NPs varies as the plasma properties vary, as do the electrostatic trapping forces. A cylindrical inductively coupled plasma (ICP) reactor was chosen for this computational investigation, a typical geometry growing NPs. A schematic of the model geometry is shown in Fig. 1 and is based on reactors used in experiments for the NP synthesis.^{57,58} The glass tube cylindrical reactor has a radius of 1 cm and a length of 8 cm, with electrically grounded boundaries for the inlet and outlet, as would occur using a metallic mesh. Power is inductively coupled into the plasma from a three-turn antenna delivering 10 W at 10 MHz with an inlet flow of Ar/SiH₄ = 98/2 at 50 SCCM. The pressure is held constant at 1 Torr by adjusting the outlet flow rate, giving an average gas residence time of 33 ms. The temperature of the inlet gases and surrounding reactor surfaces are held constant at 325 K.

Plasma properties and chemistry for the base case conditions are also shown in Fig. 1. Under steady-state operation, the electric potential in the plasma peaks at 26.7 V between the coils of the antenna at the location of maximum ion production [Fig. 1(b)]. The surface of the dielectric tube charges negatively near the coils

to -2.2 V at a minimum to balance the electron and positive ion fluxes to its surface. The on-axis ($r=0$ cm) electron density and temperature profiles are shown in Fig. 1(d). The electron density peaks close to the powered antenna ($1 > r > 0$ cm) at $8.6 \times 10^{10} \text{ cm}^{-3}$ and decreases by nearly three orders of magnitude downstream by the pump. This decrease is due to the large rate of electron dissociative attachment to silane and dissociative recombination of silane ions, both of which are sources of radicals to grow NPs. The electron temperature T_e has a maximum at 4.2 eV adjacent to the antenna [Fig. 1(c)], decreasing to 1.7 eV moving away from the antenna due to both elastic and inelastic collisions for the (relatively) high pressure of 1 Torr.

The dominant positive ion varies spatially, with SiH_3^+ being the dominant ion near the inlet (density of $4 \times 10^{11} \text{ cm}^{-3}$) where the SiH_4 density is high and SiH_3^+ can be readily produced by electron impact dissociative ionization. Close to the wall of the reactor adjacent to the antenna, Ar^+ and Ar_2^+ achieve their maximum densities of 5×10^{11} and $3 \times 10^{11} \text{ cm}^{-3}$, respectively, and decrease downstream due to charge exchange reactions. Downstream, ArH^+ and H_3^+ become the dominant positive ions with densities of 2×10^{12} and $3 \times 10^{12} \text{ cm}^{-3}$, respectively, as the density of hydrogen increases from the dissociation of silane. The dominant negative charge carrier throughout the reactor is Si_2H_5^- , with a density ranging from $2 \times 10^{12} \text{ cm}^{-3}$ upstream where power deposition is high to $5 \times 10^{12} \text{ cm}^{-3}$ downstream where a nearly fully ion-ion plasma is formed. SiH_3^- contributes to the negative charge in the powered zone between the antenna, with a density of $2 \times 10^{11} \text{ cm}^{-3}$, greater than the peak electron density.

The on-axis densities of nanoparticle precursors and growth species are shown in Fig. 1(e) for the length of the reactor. Silane flows into the reactor and dissociates by electron impact reactions primarily in the high-power deposition region between the antenna, decreasing by two orders of magnitude from its peak density of $3.8 \times 10^{14} \text{ cm}^{-3}$ upstream. Localized gas heating up to 433 K occurs near the center of the reactor resulting in gas rarefaction. SiH_2 and SiH_3 are produced from electron impact dissociation of SiH_4 , additionally producing atomic H. SiH_2 rapidly inserts into fully hydrogenated silanes and is one of the fundamental growth species in the mechanism of nanoparticle formation.⁴¹ These reactions create Si_2H_6 from SiH_4 , consuming SiH_2 in the process and leaving the density heavily localized (maximum of $1 \times 10^{12} \text{ cm}^{-3}$) where its production is at a maximum. Dehydrogenation of Si_nH_x species occurs progressively downstream from collisions with Ar excited states. Hydrogen abstraction from Si_2H_6 forms Si_2H_5 , which becomes the main silicon radical downstream with a density $2 \times 10^{14} \text{ cm}^{-3}$. In addition to reactions with silane species, H atoms can etch NPs and impact the size of trapped particles, a process not included in the model.

Pulsed periodic steady-state values for the spatially averaged electron density and electron density weighted electron temperature are shown in Fig. 2(a) for a 20 kHz pulse repetition rate (PRF) providing a pulse period of $50 \mu\text{s}$ with the power profile shown in Fig. 2(b). The average power deposition is 10 W with a duty cycle of 50% spent at peak power, with a few μs of rise and fall time. When the power first turns on, T_e spikes to an average over 5 eV and is higher in between the antenna to rapidly ionize the plasma by electron impact reactions.⁵⁹ The electric potential in the plasma spikes

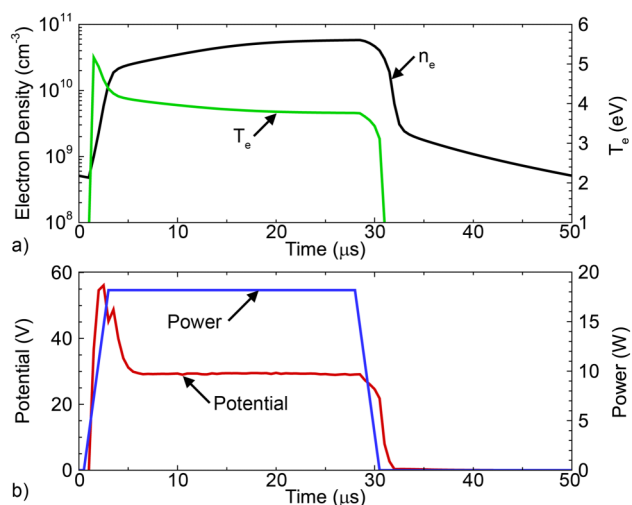


FIG. 2. Pulsed periodic properties for a $50 \mu\text{s}$ pulse with a 50% duty cycle (1 Torr, 10 W average power, 50 SCCM, $\text{Ar}/\text{SiH}_4 = 98/2$). (a) Pulsed periodic electron density and temperature and (b) power profile and maximum electric potential in the plasma.

to 57 V, higher than 26.7 V for continuous wave power, due to the low electron density and high temperature at the onset of a power pulse. When the power turns off, T_e decreases quickly due to the high collisionality at 1 Torr. With the electric potential being proportional to T_e , there is a commensurate decrease in plasma potential. Thermal electron attachment to radicals, dissociative recombination, and diffusion to the walls produce the decrease in electron density. Although the electron density decreases by a factor of 100 in the afterglow, the time rate of change decreases shortly after the power pulse ends. This is due to the decrease in electron temperature that then decreases the rate of loss by ambipolar diffusion. Since the PRF is relatively high at 20 kHz, the electron density does not have time to fully dissipate and may have some influence on the results of the particle simulation. Since the DTS model uses time-slicing, the time NPs experience is greater than in the plasma portion of the simulation. The plasma pulsing may be more akin to a high-low power pulse than strictly on-off.

The dynamics of nanoparticle growth captured in the DTS are shown in Figs. 3 and 4, comparing growth under continuous wave power (Fig. 3) and under pulsed operation (Fig. 4) for the same average power of 10 W. (These results follow the evolution of the growth of the initial NP precursors. Results for continuous generation of precursors are discussed in Sec. III D.) The images are for a series of time snapshots following initiation of the particles. The sizes of the particles are indicated by the diameter of the symbol. The symbols are color coded with charge on the particle. The pulse period is 5 ms with a duty cycle of 50%. In both cases, particles are initialized between the first two turns of the antenna. Analyzing the sequential steps of particle growth and transport is more clear when following the evolution of this burst of particles. Continuous particle generation is discussed below.

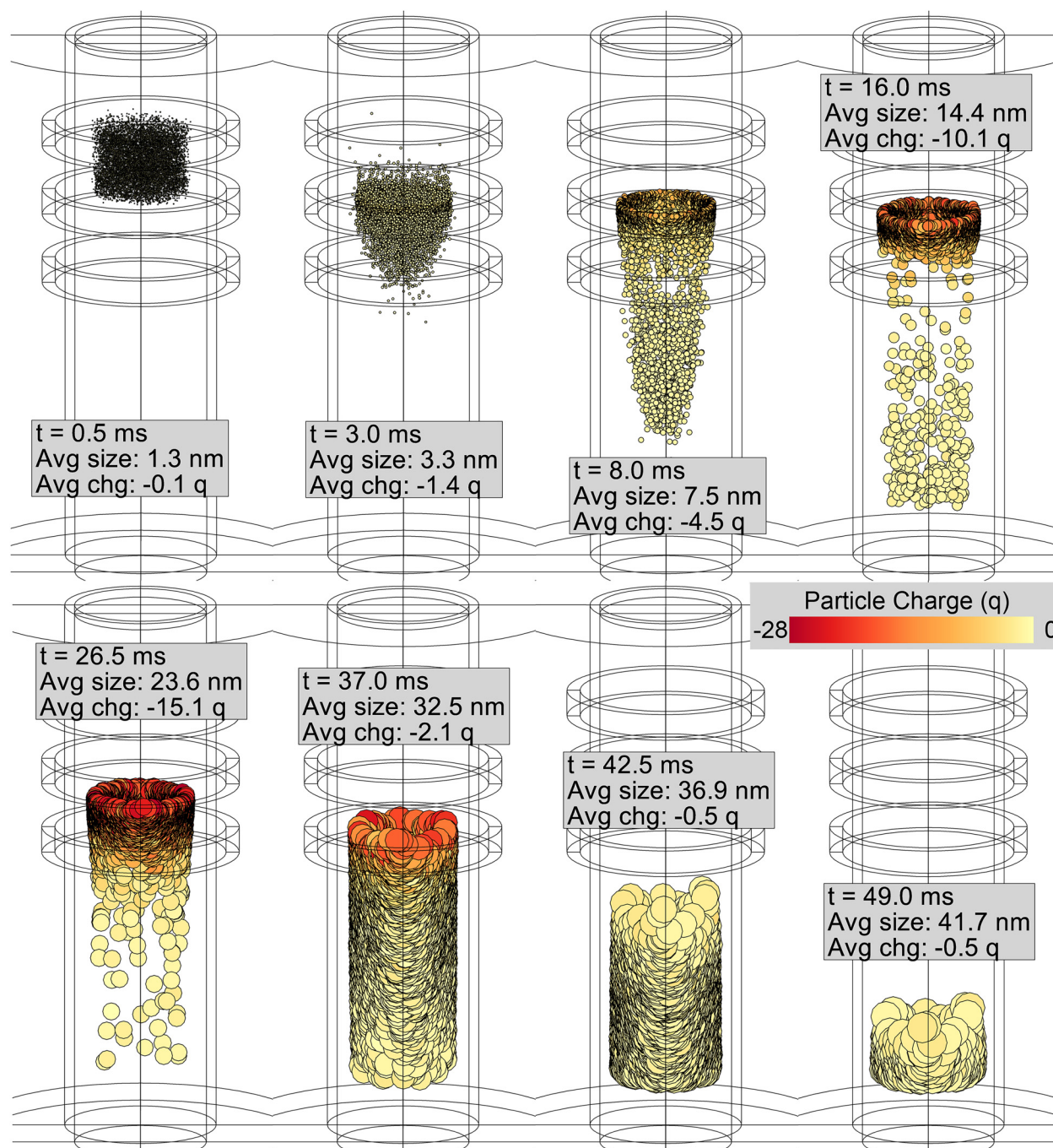


FIG. 3. Nanoparticle positions in the plasma reactor and properties for continuous wave power (10 W). Particle sizes correspond to the diameter of the symbol. Particle charge is indicated by the color of the symbol. Images are shown for different times (0.5–49 ms) after initializing the NPs. The average particle diameter and charge are shown for each time.

For continuous wave power, within a few ms, most of the particles charged to an average of $-1.4 q$ for an average particle diameter of 3.3 nm. Due to a no-slip boundary condition on the reactor walls for the fluid flow, the gas velocity profile in the reactor is

parabolic shaped, with highest velocity on-axis, decreasing toward the walls. This velocity profile contributes to particles forming a ring shape in the plasma—negative particles are trapped by the positive plasma potential that peaks off-axis, while particles

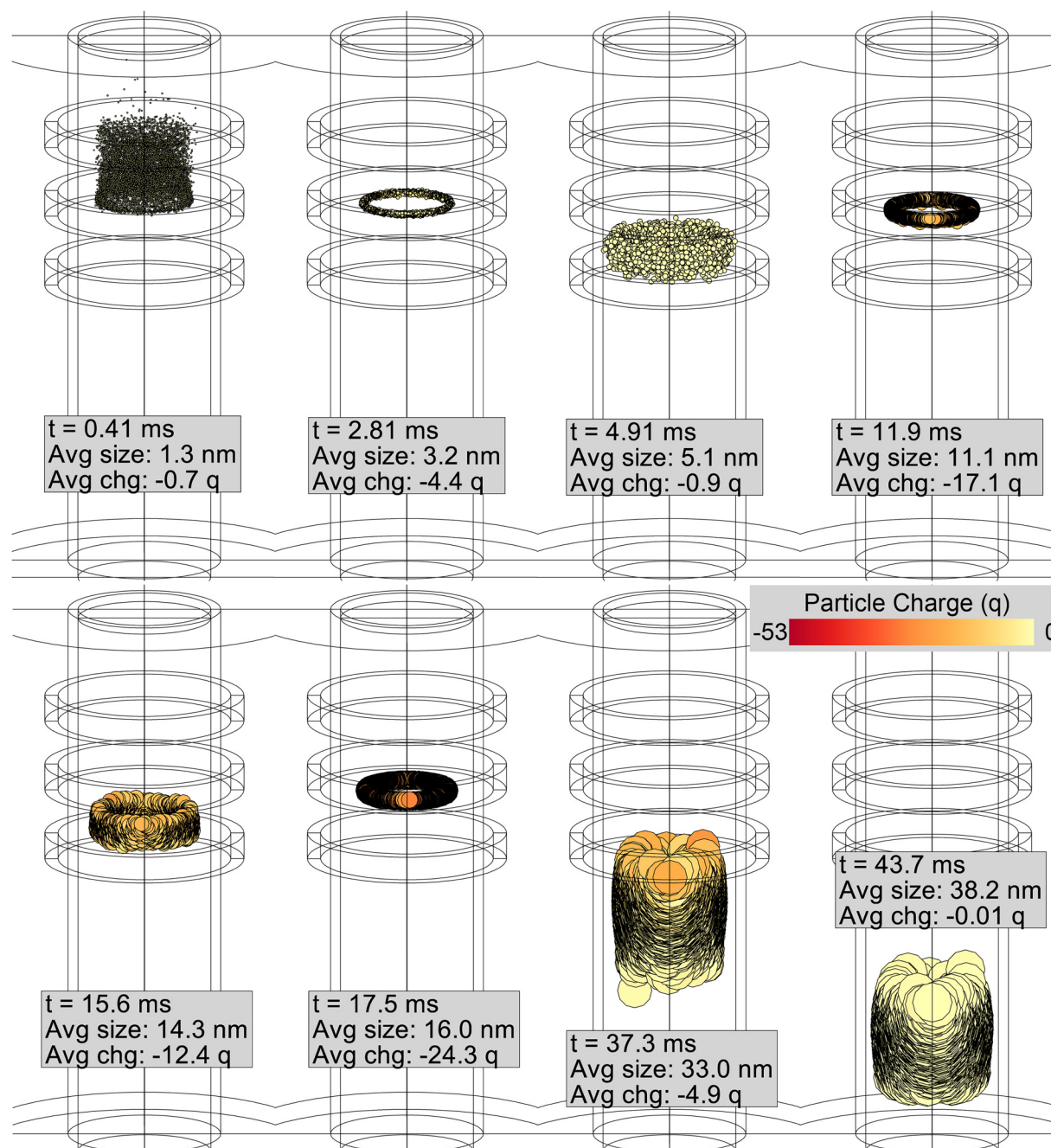


FIG. 4. Nanoparticle positions in the plasma reactor and properties for pulsed plasma conditions (10 W average power, 50% duty cycle, 5 ms pulse approximated by time slicing). Particle sizes correspond to the diameter of the symbol. Particle charge is indicated by the color of the symbol. Images are shown for different times (0.4–44 ms) covering several pulses after initializing the NPs. The average particle diameter and charge are shown for each time. Using pulsed power leads to more negative particle charge during the power on portion of the cycle and increased trapping compared to continuous wave power.

on-axis are more rapidly accelerated downstream on-axis by the higher flow speed ($t = 8$ ms). The plasma potential is 0.4 V more positive in a torus centered under the coils, thereby providing a deeper trap for negative particles.

Thermophoresis can be a dominant force acting on particles in plasmas, driven by macroscopic gradients in gas temperature. This is particularly the case in the afterglow of plasmas where electrical forces dissipate, whereas the gas temperature and its gradients

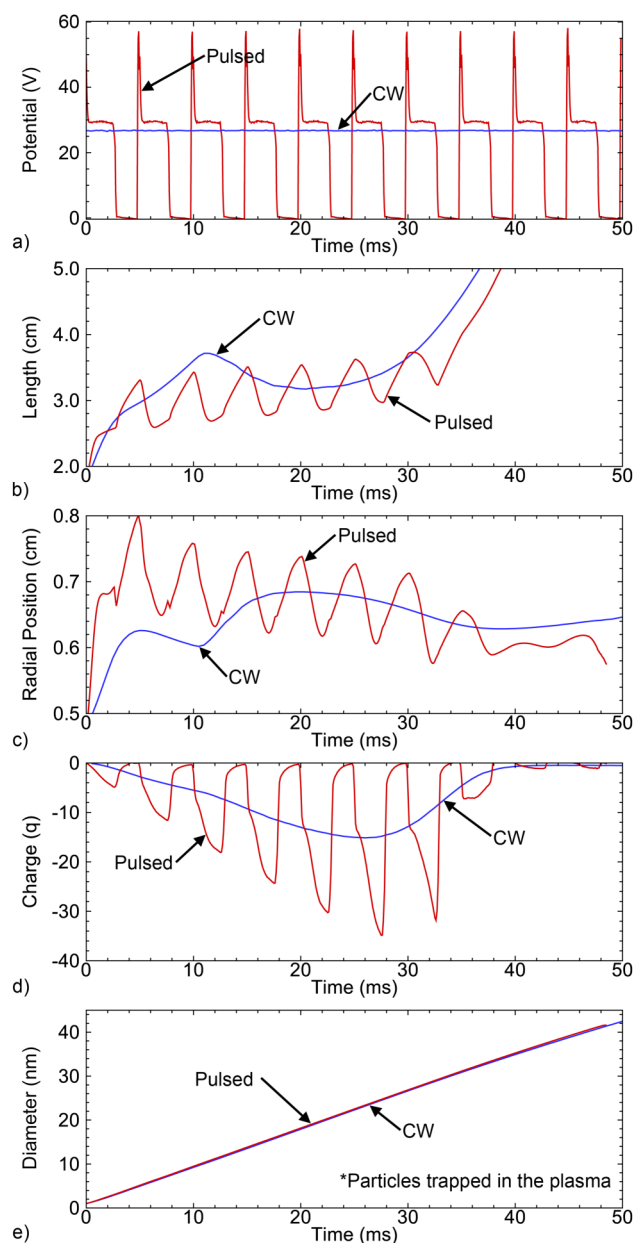


FIG. 5. Time resolved properties of the plasma and nanoparticles for pulsed (red) and CW (blue) plasma excitation. Values for particle properties are averaged over the nanoparticles currently in the reactor. (a) Maximum plasma potential, (b) average axial position of the NPs (length is measured from the inlet), (c) average radial position of the NPs, (d) average charge on the NPs, and (e) the average particle diameter as a function of time the particles are in the plasma.

remain constant in comparison. For these results, the temperature of the glass tube was held constant at 325 K while the gas temperature is >325 K. So the temperature gradient toward the wall will on the average always be negative. The thermophoretic force will,

therefore, on the average, point from the plasma toward the walls. This force would tend to de-trap particles. If the temperature of the glass is allowed to increase, the temperature gradient from the plasma to the wall will still be negative in order to convect heat from the plasma to the walls, which would still act to de-trap particles.

Particles continue growing to an average radius of 14.4 nm and charging negatively $-10.1q$ on average by 16 ms. At $t = 26.5$ ms, the majority of particles are still trapped by the plasma potential and are on average 23.6 nm in radius with a charge of $-15.1q$. The axial location at which the particles are trapped slowly moves downstream up to this time due the increasing fluid drag forces afforded by the larger particles. By $t = 37.0$ ms, the average particle radius increases to an average of 32.5 nm and the force due to fluid drag begins to dominate over electrostatic trapping. At this time, the trap is emptied and particles begin to flow downstream. Due to the steep gradients in charged species densities and temperatures, moving downstream shifts the dominant negative current to the particles from hot light electrons to cold heavy ions. The particles then begin to neutralize in a decreasing electric field. The end result is that the electrostatic force dissipates, leaving fluid drag as the dominant force. Particles acquire the speed of the local gas flow, leaving the reactor at 49 ms with an average radius of 41.7 nm.

NP growth and transport dynamics using pulsed power are shown in Fig. 4. Particles were initialized in the plasma at the onset of a pulse. The maximum electric potential in the plasma is plotted as a function of time in Fig. 5(a). The average location of NPs in the axial direction is shown in Fig. 5(b) and in the radial direction in Fig. 5(c). Average charge on the NPs as a function of time is shown in Fig. 5(d), and diameter is shown in Fig. 5(e). The CW values are shown for reference in each image. Referring to Fig. 4, at $t = 2.81$ ms, the power for the first pulse is still on and the particles have grown to a diameter of 3.2 nm with an average charge of $-4.4q$. The particles are more negatively charged compared to particles grown under CW conditions at a similar time and size. The number of charges on the particle is largely determined by the magnitude of the electrical floating potential that is proportional to electron temperature. The average higher T_e during the power-on portion of the pulse then produces a larger (negative) floating potential and larger (more negative) charge on the NP. The electrostatic trapping force on the particles during the power-on portion of pulsing is greater due to the more negative charge on the NP and more positive plasma potential compared to CW power. The end result is that the trapping location is a more finely defined torus compared to CW power, having a larger average radial position [Fig. 5(c)].

As the power decreases, particles quickly discharge to an average charge near 0 [$t = 4.91$ ms, Figs. 4 and 5(d)]. When the NPs are small (a few nm), there is the possibility that charging might statistically be positive.^{33,34} In these simulations, we observe few (if any) positively charged NPs. In the absence of a trapping force due to the positive plasma potential, particles move downstream in response to a fluid drag (greater length) and spread radially inwards and outwards with the average radius decreasing. When the power turns back on at $t = 5$ ms, the electron temperature increases and the positive electric potential is re-established.

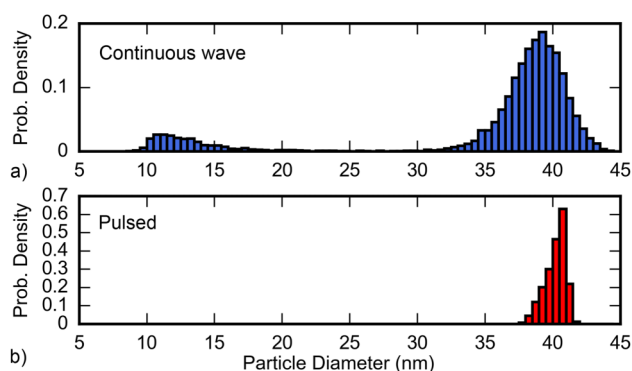


FIG. 6. Particle size distributions for particles leaving the reactor for (a) continuous wave power and (b) for pulsed conditions (5 ms pulse, 10 W average power, 50% duty cycle). These results correspond to the conditions shown in Figs. 3 and 4. The histograms of the raw data ($N \approx 10\,000$ particles, bin width of 0.5 nm) were scaled to a probability density for comparison.

Particles re-charge negatively and are accelerated upstream against the bulk fluid flow toward the electrostatic trapping zone (small length). Particles drift outward from the axis and inward from the walls, toward a more positive electric potential in the plasma, again forming a ring ($t = 11.9$ ms). The particles are now larger (diameter = 11.1 nm) with a larger, more negative charge ($-17.1q$).

This process of particles charging negative when the power is turned on and becoming trapped upstream in the plasma, followed by discharging and flowing downstream when the power is turned off, repeats for approximately seven cycles. With each cycle, the NPs grow larger, are more susceptible to fluid drag forces, and so are trapped deeper in the reactor (larger length). If the plasma properties at the trapping location for each pulse were the same, you would expect the (negative) charge to increase each cycle as the NPs grow larger. This trend occurs up to the sixth cycle for which the most negative NPs are produced ($-36q$). On the seventh cycle, the trapping location is on the fringe of the power deposition zone where the electron temperature is beginning to decrease. In spite of the NPs being larger than on the sixth cycle, the charge on the seventh cycle is less negative ($-32q$). At $t = 37.3$ ms on the eighth cycle when the power is on, particles are on average 33 nm in diameter but charge only to $-4.9q$ due to fluid drag transporting the particles downstream where both the electron temperature and density are lower. Beyond the eighth cycle, the particles are far enough downstream that they do not significantly charge when the power turns on, coupled with the particles being larger and more susceptible to fluid drag. At this point, pulsing has a small effect on the transport of particles as they are entrained in the flow and leave the reactor.

Statistics were collected on NPs as they flow out of the reactor. The distributions of NP diameters for CW and pulsed power are shown in Fig. 6. These distributions result from collecting 10 000 particles into diameter bin widths of 0.5 nm. For CW conditions, nanoparticles that were trapped in the plasma prior to being entrained in the gas and flowing out of the reactor have a near-normal distribution about a mean of a diameter of 39 nm

with a standard deviation of about 2 nm. However, not all particles were trapped (or were momentarily trapped), leading to a second peak in the probability distribution at around 12 nm. These particles flow out of the plasma a short time after being seeded, a consequence of stochastic charging. Particles that charge positive will experience the opposite effect of trapping since the axial electrostatic force points downstream and to the walls. (This rapid loss of positive particles may also explain their low density.) The particles having smaller diameters may also have been statistically closer to the axis where the gas flow speed is higher, producing a larger fluid drag force. Particles that transport a few cm downstream from the peak in the plasma potential will likely not recover to become trapped for these plasma conditions. Downstream of the peak in the plasma potential, the plasma is highly electronegative (small electron density) with a low electron temperature that will not re-charge particles enough to become trapped.

The NP size distribution leaving the reactor when using pulsed power is shown in Fig. 6(b). This distribution is also for a bin width of 0.5 nm with $N \approx 10\,000$ particles collected. The collected particles have a more narrow size distribution, 5 nm wide peaking at a diameter of 41 nm, than for the CW plasma. The

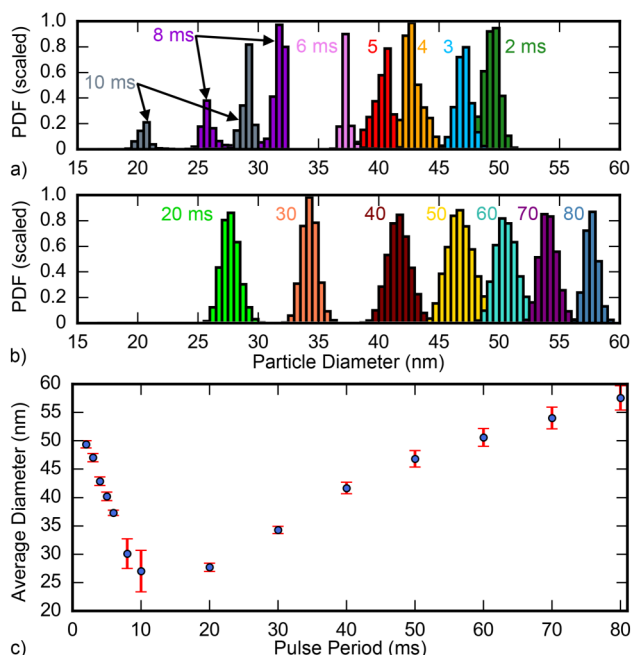


FIG. 7. Size distributions of the NPs collected leaving the reactor for different pulse periods ranging from (a) 2 to 10 ms, where the distributions shift to smaller sizes with increasing pulse period, and (b) 20 to 80 ms, where the size distributions shift to larger sizes with increasing pulsed period. The average values are plotted in (c) with the bars indicating a standard deviation in particle size. The wide bars for 8 and 10 ms are due to bimodal distributions, indicating a large degree of customization available with pulsing. The probability density functions of particle size ($N \approx 10\,000$ particles, bin width of 0.5 nm) were scaled for convenience.

irregular shape of the distribution comes from there being striations in particle density at the end of a pulse. As the particles leave the electrostatic trapping zone, particles closer to this zone may become negatively charged when the power turns on again and becomes partially trapped. These results suggest that using pulsed power may be a method to modify or tune the NP size distribution, in this case increasing mono-dispersity in particle sizes.

The ability to tune the NP size distribution with pulsed power, discussed in more detail below, is clearly a function of the pulse power format. For example, consider comparing NPs grown using CW and pulsed processes using the same average power. During the power-on period, the instantaneous power is higher during pulsing than during CW operation. As a result, electrostatic trapping is more likely due both to higher (positive) peak electrical potential in the plasma and more negative charge on the NPs [Fig. 5(d)]. The production of growth species (e.g., silane radicals) differs little between CW and pulsing since their densities depend largely on average power that is the same. With the densities of growth species being nearly the same, the average growth rates of NPs using the same average power, pulsed or CW, are essentially the same. As a result, the NPs will be approximately the same size as long as the NPs are trapped in the plasma [Fig. 5(e)]. However, the time spent in the plasma is a function of pulsing, which then translates to a different distribution of NP sizes. Using pulsed power may widen the parameter space of viable conditions to grow nanoparticles by increasing the trapping potential.

B. Effects of pulse period/pulse repetition frequency

The pulse period (inverse of PRF, pulse repetition frequency) is the time required for a full power pulse to repeat. To isolate the effects of the pulse period on nanoparticle growth, time slicing of the same 50 μ s power pulse as shown in Fig. 2 was used to approximate varying pulse lengths on NP growth without greatly changing charged species densities or neutral chemistry. This method provided effective pulse periods ranging from 2 to 80 ms (10 W average power, 50% duty cycle).

Results from the DTS are shown in Fig. 7 for probability distribution function (PDF) for particle diameter and average diameter. The PDF for a 5 ms long pulse was compared to CW operation with the same average power in Fig. 6, and similar size NPs were produced—the PDFs were spread around a diameter of 40 nm. The results in Fig. 7 show that shorter pulses (higher repetition rates) produced PDFs having a mean diameter increasing for shorter pulses. Pulses of 4 ms (250 Hz), 3 ms (333 Hz), and 2 ms (500 Hz) produced mean diameters of 43, 47, and 49 nm, respectively. Shorter pulses resulted in there being shorter power-off periods allowing less time for particles to flow downstream from the trapping zone in the plasma. The trapping potential remains higher (more positive) than with CW power and manifests as monodisperse distributions. Pulsing may be a method to increase particle sizes over similar conditions with CW power, while increasing particle mono-dispersity.

Increasing pulse length (decreasing PRF) reduced particle diameter. The 6 ms pulse period (167 Hz) produced the most monodisperse PDF centered around 37 nm—smaller particles than

for CW and the base case 5 ms (200 Hz) pulse. This result implies that there is an optimum PRF if monodisperse distributions are the goal. Longer pulse periods of 8 ms (125 Hz) and 10 ms (100 Hz) produced bi-modal PDFs—a consequence of particles becoming striated when the power turns on, with some particles becoming trapped for another pulse while others continue to flow out of the reactor. Since particles are seeded at the onset of a pulse, it is highly likely that they are trapped for half of the pulse period (50% duty cycle \times pulse period). For the 10 ms pulse, the smaller peak in the PDF at 20 nm results from particles that were trapped only for the initial 5 ms when the power was first turned on. The peak in the PDF at 28 nm comes from particles that were again caught in the trap on the second pulse and spent (at a minimum) 5 ms more trapped in the plasma zone. The PDF for the 8 ms pulse shows a similar trend; however, particles are trapped for two or three pulses rather than just one due to the shorter pulse period. As a result, the bimodal peaks in the PDF are closer together than for the PDF resulting from the 10 ms pulse.

For these conditions, the 10 ms pulse trapped particles for one or two pulses. Operating with longer pulse periods (lower PRF), one would expect particles to remain trapped for only a single pulse. As expected, increasing the pulse period increases the average particle size as shown in Fig. 7(b). For longer pulse periods (lower PRF), particles remain in the trapping zone until the power turns off, providing direct control over how long particles spend growing by surface radical deposition. These longer pulses produce monodisperse PDFs with mean diameters ranging from 28 to 58 nm. The particle diameters can be larger than under CW operation for the same average power because the trapping potential when the power is on is akin to operating at double the power. However, the monodisperse distributions arise, in part, from seeding the particles only at the beginning of the pulse. If particles were continuously formed, one might expect broader distributions skewed to have smaller particle size.

The ability to tune particle PDFs using the pulse period is summarized in Fig. 7(c), where the average particle diameters for as a function of pulse period are shown. The bars for each point indicate a standard deviation, with large wide bars indicating the presence of dual-peaked PDFs, increasing natural spread in the distribution, or outliers. The wide bars for 8 and 10 ms pulse periods result from bimodal distributions. Under CW operation, the average particle diameter for trapped particles is 39 nm. Using pulse power provides a method to customize the mean size by nearly 50% in both directions (larger and smaller).

The pulse periods that provide flexibility in particle diameter relative to CW operation will heavily depend on the gas residence time. The important factors to consider are the size of the trapping region in the plasma, the gas velocity or residence time, and the pulse period. For longer gas residence times, particles will move downstream from the trapped zone at a slower rate and longer plasma pulses may be beneficial. If particles move too far downstream from the high plasma density region when the power is turned off, they will likely not charge negative (or not recharge to their prior state) when the power turns on again. As a result, the electrostatic force during the power pulse may not dominate over the fluid drag force, and the particles may not be re-trapped. Using these guidelines, it should be possible to estimate pulsing times for specific systems that could provide beneficial tuning of the NP properties.

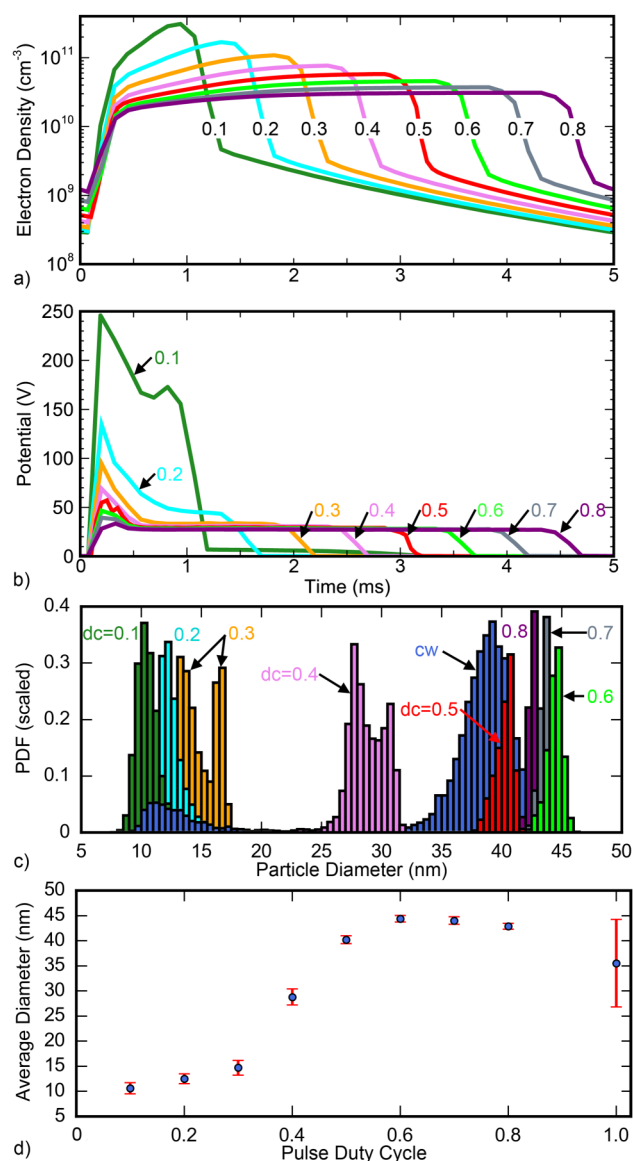


FIG. 8. Plasma properties and NP diameters for different power pulse duty cycles while holding the pulse period (5 ms) and average power (10 W) constant. (a) Electron density, showing increased peak density with decreasing duty cycle, (b) increasing peak in the plasma potential with decreasing duty cycle, (c) size distributions (scaled) of the NPs collected leaving the reactor, and (d) average particle diameter with standard deviation bars. Note that 5 ms pulses were modeled in the DTS, and the time scales in (a) and (b) are in the NP frame of reference.

C. Effects of pulse duty cycle

The pulse duty cycle is defined as the ratio of time spent with the power on compared to the total pulse period. To achieve the same average power, the peak power during the power-on part of

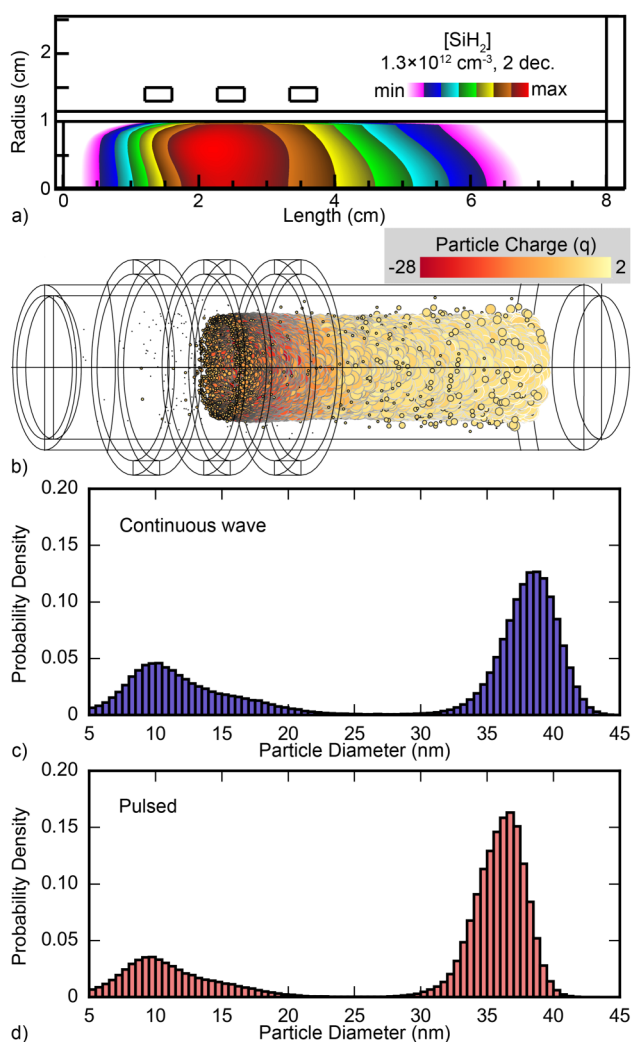


FIG. 9. Plasma and NP properties when using continuous particle seeding with CW power. (a) The SiH_2 density, used to determine seeding location probabilities in the DTS, (b) the steady-state output distribution of NPs (symbol size indicates diameter and symbol color indicates charge), (c) size distributions of the NPs collected leaving the reactor for continuous power, and (d) NP distributions for pulsed conditions (5 ms pulse, 10 W average power, 50% duty cycle).

the period scales inversely with the duty cycle. The end result is that shorter duty cycles have higher power applied during a shorter time, leading to larger spikes in electron density and electric potential in the plasma, as shown in Fig. 8. To investigate the consequences of the duty cycle, the same procedure was followed as discussed in Sec. II. $50 \mu\text{s}$ plasma pulses (with duty cycles ranging from 0.1 to 0.8) were simulated in the HPEM until a pulsed periodic steady state was reached. At that time, the DTS was executed for several pulses with time-slicing to model particle dynamics with 5 ms pulses.

PDFs from the results of the DTS are shown in Fig. 8(c) for duty cycles of 0.1–0.8 for 5 ms pulse periods (200 Hz). Narrow PDFs were produced for duty cycles greater than 0.5, resulting in average diameters that are greater than those produced by CW operation. The average particle diameters for these PDFs are all within a few nm of each other. Having the power be on for additional fractions of a ms can make the difference between particles being trapped for an extra pulsed cycle or not. Other factors such as changes in the peak electron density and potential play less of an important role on the overall size distributions of particles for a given pulse period provided that the average power is constant. There are even benefits obtained by pulsing even at a duty cycle of 0.8 (80% of the time spent at peak power with the rest of the time ramping the power up and down) compared to CW power—more uniform PDFs with slightly larger particle size.

PDFs for lower duty cycles are also shown in Fig. 8(c). With a duty cycle of 0.4, the average particle diameter decreases to 29 nm with a larger spread compared to the base case of a duty cycle of 0.5. Lower duty cycles (0.1, 0.2, and 0.3) have the power on only long enough to trap the particles for a single pulse (or two, as seen by the second peak in the PDF at 17 nm for duty cycle of 0.3). The average particle diameters for duty cycles of 0.1–1.0 (CW) are shown in Fig. 8(d). For a given pulse period (in this case 5 ms), choice of the duty cycle results in particles being trapped for many pulses ($dc = 0.5\text{--}0.8$) or for only one pulse ($dc = 0.1\text{--}0.3$). There

may only be a small range of duty cycles (for a given pulse period) where particles are trapped for an intermediate number of pulses. These trends indicate that the pulse period (or pulse repetition frequency) may be the most effective first-order control mechanism for PDF, while the pulse duty cycle may be better for fine tuning particle properties. The physics at play are the same—particles can be trapped in the plasma when the power is on, and changing the duty cycle changes the ratio of time particles spend trapped compared to be dominantly affected by fluid drag. For longer duty cycles, where particles are trapped for multiple pulses, the small changes in electron density and electric potential in the plasma have only a small effect on particles produced in the plasma.

D. Continuous particle seeding

One aspect of the results discussed above is that particles were initialized at the beginning of the simulation and tracked over time. The motivation was to less ambiguously track the particle dynamics from birth to collection—such as being able to count the number of pulsed period particles are trapped. Since pulsing is periodic, the specific time during a pulse when particles are initialized may have an impact, particularly for longer pulses with pulse periods near the gas residence time. It was also assumed that particles spawn in a set location between the first and second antenna turns. Both assumptions were tested by allowing for continuous particle

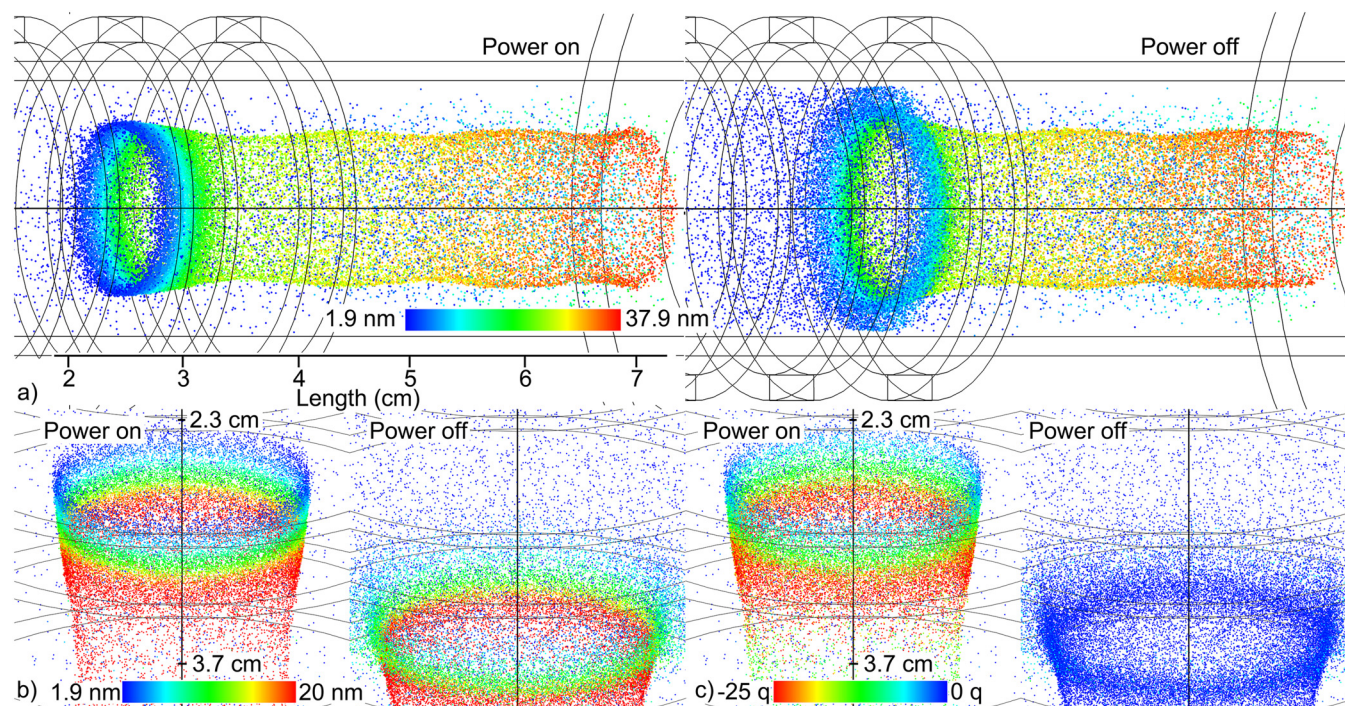


FIG. 10. Plasma and NP properties when using continuous particle seeding and pulsed power (5 ms pulse, 10 W average power, 50% duty cycle). (a) Particle distributions in the reactor (left) at the end of the power-on portion of the pulse and (right) at the end of the power-off portion of the pulsed. The particle diameters are indicated by the colors of the symbols (1.9–38 nm). (c) Particle locations during power-on and power-off in the power deposition region between the antenna with color indicating diameter (1.9–20 nm) and (c) with color indicating charge (0–25 q).

seeding throughout the pulse period, with initialization locations scaled to the spatial density of SiH_2 —one of the major growth species for NPs—whose density is shown in Fig. 9(a). SiH_2 readily inserts into fully hydrogenated Si_xH_y and so is consumed quickly after being formed by electron impact dissociation of SiH_4 . These processes produce a density of SiH_2 localized within the antenna, with a maximum of $1.3 \times 10^{12} \text{ cm}^{-3}$, decreasing by two orders of magnitude near both the inlet and the pump. Based on this distribution, assuming particles are seeded between within the bounds of the antenna is reasonable.

For CW operation, 10 000 particles were initialized in the plasma with a radius of 0.5 nm and zero charge using the spatial

distribution of SiH_2 . Particles were continuously replaced into this spatial distribution when particles were lost by flowing out of the system. This process was continued until the spatial distribution [Fig. 9(b)] and size distribution [Fig. 9(c)] reached steady-state values. Achieving the steady state resulted in collecting >300 000 particles.

In the steady-state, a natural spatial afterglow forms in the plasma. A spatial afterglow is the recombination (or decrease in electron density) along a flow direction downstream of a plasma, in analogy to a temporal afterglow that occurs over time following a pulsed plasma. In this spatial afterglow, NPs downstream of the plasma are almost all neutral charged due to currents to the particles being dominated by both cool positive and negative ions,

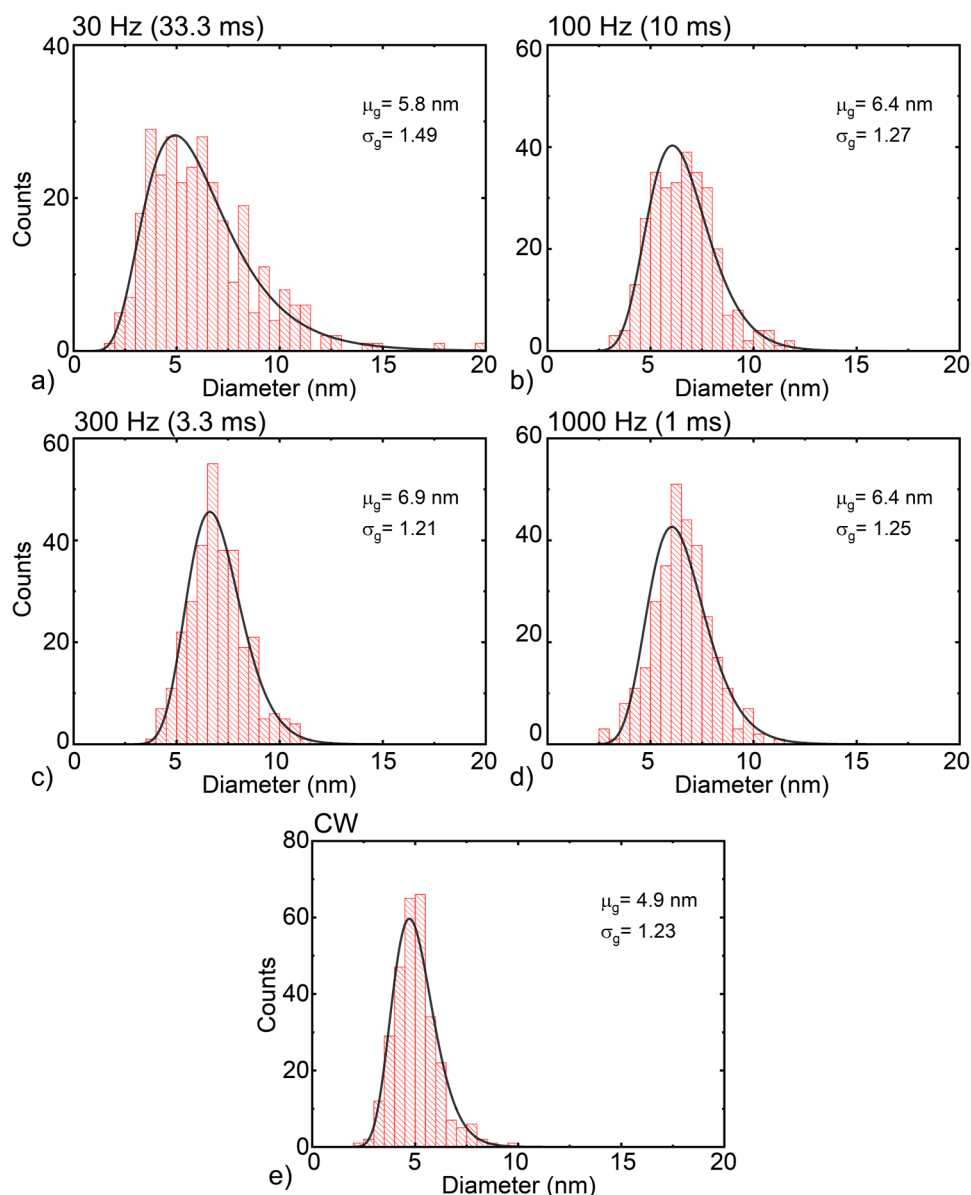


FIG. 11. Experimental particle distribution functions for a flowing Ar/SiH₄ plasma for pulsed operation with an average power of 10 W, a duty cycle of 50%, and pulse repetition frequencies of (a) 30, (b) 100, (c) 300, and (d) 1000 Hz. (e) Particle distribution function for CW excitation.

rather than hot electrons. Within the small cm-sized trapping zone between the antenna, there is a clear gradient in particle sizes with smaller particles being trapped closer to the peak plasma potential (upstream near the inlet) and larger, more negative charged particles further downstream near the pump, as shown in Fig. 9(b). This is a natural consequence of the fluid drag force scaling more with particle size than the electrostatic trapping force. For CW power, the distribution of particle sizes is similar when comparing continuous vs static particle seeding [Figs. 9(c) and 6(a)]. The distribution features two peaks—one centered around 38 nm resulting from particles trapped in the plasma for several tens of ms and another near 10 nm resulting from particles that are not trapped (or not trapped for a long time). Since particles are initialized according to the SiH_2 density (rather than constrained to being initialized between the antenna), some of these particles are initialized outside the trapping zone. More small particles are created overall and the peak of small particles is larger than under CW conditions.

For the 5 ms, 50% duty cycle pulsed plasma, 50 000 particles were initialized in the plasma and reseeded when lost. More particles were used so fewer pulses were required to obtain similar statistics in the distributions, and >700 000 particles were collected flowing out of the reactor. The particles (charge and size) in the reactor are shown in Fig. 10. The PDF for these conditions is in Fig. 9(d) and should be compared to the PDF produced by static seeding shown in Fig. 6(b). With continuous seed during the pulsed cycle, there is a second peak in the PDF consisting of small particles centered around 10 nm. These are particles that were not trapped by the plasma. Some of the population in this small-diameter peak in the PDF can be attributed to particles being initialized far outside of the trapping region where the electron density is low and do not charge negative enough to be trapped when the power turns on. The peak in the PDF corresponding to trapped particles has shifted to an average diameter of 37 nm compared to 41 nm for static seeding. This shift is likely a consequence of particles no longer being seeded when the power first turns, a condition that results in particles not being trapped for the entire duration of the power prior to particles flowing downstream when power is turned off. This partial trapping results in the PDF having a broader extent, with particles on average likely being trapped for one fewer pulse. The ratio of trapped particles with large size to un-trapped, small particles is larger with pulsed operation, a possible benefit for using pulsed power over CW power.

The dynamics captured in the DTS for the 5 ms, 50% duty cycle pulsed case with continuous particle seeding are shown in Fig. 10. Particle positions are plotted with the color indicating particle size [Figs. 10(a) and 10(b)] or charge [Fig. 10(c)]. When the power is on, particles form a ring in the trapping zone ordered from 1.9 to 20 nm. Particles are negatively charged, ranging from $\approx -1q$ up to $-25q$ for larger particles. When the power turns off, particles move radially outward and discharge, with an average charge of $\approx 0q$. Pulsing appears to cause radial compressions in the particle positions as they move downstream, spaced coinciding to the power pulses.

IV. EXPERIMENTAL CONFIRMATION OF PREDICTED TRENDS

A limited series of experiments was performed to confirm the trends predicted by the model. Silicon NPs were synthesized in a

capacitively coupled cylindrical RF discharge sustained in a 1.3 Torr mixture of $\text{Ar}/\text{SiH}_4 = 99.17/0.83$ (71.4 SCCM/0.6 SCCM) having an average power of 10 W. The apparatus is similar to that discussed in Ref. 36. The tube had an inside diameter of 2.2 cm and a total length of 19 cm, producing a residence time of 11 ms. The two ring electrodes were centered 13 cm from the gas injection location, with the electrodes separated by 2 cm. NPs were collected in a transmission electron microscope (TEM) grid 27 cm downstream of the electrodes. NPs were synthesized using CW power and pulsed power. The pulsed power consisted of a duty cycle of 50% and PRFs of 30, 100, 300, and 1000 Hz.

Experimental particle size distributions are well approximated by log-normal distributions and are shown in Fig. 11 for CW and pulsed excitation. With CW excitation, the geometric mean NP diameter is 4.9 nm with a geometric standard deviation $\sigma = 1.23$ and particles synthesized up to about 9.5 nm. With a PRF of 1000 Hz (pulsed period 1 ms), the distribution of NPs extends toward larger particles than with CW excitation, up to 11 nm. With the residence time determined by the gas flow being 11 ms, particles flow only about 5% of the reactor length during the pulse power afterglow. This enables a small amount of re-trapping and produces somewhat larger particles. With lower PRF and longer pulse periods, the tail of the particle distribution extends to larger diameters as the re-trapping enables extension of the average resident time. For a PRF of 300 Hz (3.33 ms pulse period), NPs are produced up to 12 nm; and for a PRF of 100 Hz (10 ms period), NPs are produced up to about 13.5 nm.

With a PRF of 30 Hz, the pulsed period is 33.3 ms, and the afterglow is 16.7 ms, which is now commensurate with the gas residence time. For these conditions, the afterglow is longer than the residence time, which enables the majority of particles to flow out of the reactor during the afterglow. However, those particles that statistically are charged for a longer period or are near walls where the linear flow speed is lower will not flow out of the reactor. These particles will be re-trapped, enabling several pulsed periods of growth. NPs for these conditions are grown up to 20 nm in diameter. There are gaps, or periodicity, in the particle sizes, particularly at larger particles. These gaps may be a result of particles being synchronously re-trapped for several cycles.

V. CONCLUDING REMARKS

In inductively coupled plasmas, power is deposited within a skin depth the antenna, producing high-temperature electrons and creating a maximum in the electric potential. Negatively charged nanoparticles (NPs) in the plasma experience an electrostatic force toward the volume with the high positive potential and can become trapped. Recent works have shown that this type of particle trapping in the plasma may be an important mechanism of NP growth, where particles can continue to grow by surface deposition of radical species. When a critical particle size is reached, the force due to fluid drag overcomes the electrostatic trapping force, particles flow out of the high plasma density, high plasma potential trapping zone, and eventually flow out of the reactor. Results from a computational investigation into how pulsing the plasma can manipulate this trapping zone and the resulting effects on the dynamics of nanoparticle growth were discussed.

When controlling for power, pulsing can (temporarily) create higher density plasmas with higher average electron temperatures and higher plasma potentials, which can charge NPs in the trapping region more negative than under continuous wave (CW) operation. This temporary, but strong trapping may have benefits when compared to operating with CW power, for instance, being able to create more monodisperse particle size distributions. This work qualitatively shows that pulsing the power can enable tuning the particle size distributions by effectively controlling the length of time particles remain (and can grow) in the plasma by controlling their electrostatic trapping. Ultimately, the factors that come into play in being able to tune the particle properties are the size of the trapping zone, the local gas velocity or residence time, and the duty cycle (the fractional time during the pulse period that power is on). If particles are allowed to flow downstream outside of the powered trapping zone between power pulses, the particles may be unable to charge negative and become trapped again when the power is turned on the following cycle. This is not necessarily a bad thing—power can be turned off after a certain time to produce NPs with a tunable smaller size.

With power pulsing alone, particles were able to move nearly a cm downstream between power pulses while still being trapped from pulse to pulse. This observation lends credence to the idea of having additional control schemes to move particles around the reactor based on electrostatic trapping. Decoupling the plasma source power and charged species densities from the trapping potential may be possible using separate powered electrodes and could lead to advances in complex nanoparticle production using low-temperature flowing plasmas.

Note added in proof. The authors recently became aware of the study by Schwan et al. [<https://doi.org/10.1088/1361-6463/ac3867>] on pulsed plasma operation for production of nanoparticles. The results of that study appear consistent with our findings.

ACKNOWLEDGMENTS

This work was supported by the Army Research Office MURI under Grant No. W911NF-18-1-0240, the National Science Foundation (NSF) (Nos. IIP-1747739 and PHY-2009219), and the Department of Energy Office of Fusion Energy Science (No. DE-SC0020232).

AUTHOR DECLARATIONS

Conflict of Interest

The authors have no conflicts to disclose.

Author Contributions

Steven J. Lanham: Conceptualization (equal); Data curation (equal); Formal analysis (equal); Investigation (equal); Software (equal); Visualization (equal); Writing – original draft (equal). **Jordyn Polito:** Data curation (supporting); Investigation (supporting); Software (supporting); Writing – review and editing (supporting). **Zichang Xiong:** Validation (equal); Visualization (supporting); Writing – review and editing (supporting). **Uwe R. Kortshagen:** Funding acquisition (equal); Project administration (equal); Validation (equal); Writing – review and editing

(supporting). **Mark J. Kushner:** Conceptualization (equal); Funding acquisition (equal); Project administration (equal); Supervision (equal); Writing – review and editing (equal).

DATA AVAILABILITY

The data that support the findings of this study are available within the article and available from the corresponding author upon reasonable request.

REFERENCES

- ¹U. Kortshagen, *J. Phys. D: Appl. Phys.* **42**, 113001 (2009).
- ²A. Bapat, C. Anderson, C. R. Perrey, C. B. Carter, S. A. Campbell, and U. Kortshagen, *Plasma Phys. Control. Fusion* **46**, B97 (2004).
- ³U. R. Kortshagen, R. M. Sankaran, R. N. Pereira, S. L. Girshick, J. J. Wu, and E. S. Aydil, *Chem. Rev.* **116**, 11061 (2016).
- ⁴C. R. Gorla, S. Liang, G. S. Tompa, W. E. Mayo, and Y. Lu, *J. Vac. Sci. Technol. A* **15**, 860 (1997).
- ⁵A. Izadi and R. J. Anthony, *Plasma Process. Polym.* **16**, e1800212 (2019).
- ⁶L. Mangolini, E. Thimsen, and U. Kortshagen, *Nano Lett.* **5**, 655 (2005).
- ⁷A. Alvarez Barragan, N. V. Ilawe, L. Zhong, B. M. Wong, and L. Mangolini, *J. Phys. Chem. C* **121**, 2316 (2017).
- ⁸E. Thimsen, U. R. Kortshagen, and E. S. Aydil, *J. Phys. D: Appl. Phys.* **48**, 314004 (2015).
- ⁹B. L. Greenberg, S. Ganguly, J. T. Held, N. J. Kramer, K. A. Mkhoyan, E. S. Aydil, and U. R. Kortshagen, *Nano Lett.* **15**, 8162 (2015).
- ¹⁰A. Ho, R. Mandal, R. R. Lunt, and R. J. Anthony, *ACS Appl. Nano Mater.* **4**, 5624 (2021).
- ¹¹B. Ramamurthi and D. J. Economou, *J. Vac. Sci. Technol. A* **20**, 467 (2002).
- ¹²D. J. Economou, *J. Phys. D: Appl. Phys.* **47**, 303001 (2014).
- ¹³L. Xu, D. J. Economou, V. M. Donnelly, and P. Ruchhoeft, *Appl. Phys. Lett.* **87**, 041502 (2005).
- ¹⁴S. Samukawa, *Appl. Phys. Lett.* **64**, 3398 (1994).
- ¹⁵H. Shin, W. Zhu, L. Xu, V. M. Donnelly, and D. J. Economou, *Plasma Sources Sci. Technol.* **20**, 055001 (2011).
- ¹⁶S. Banna, A. Agarwal, G. Cunge, M. Darnon, E. Pargon, and O. Joubert, *J. Vac. Sci. Technol. A* **30**, 040801 (2012).
- ¹⁷S. Banna, A. Agarwal, K. Tokashiki, H. Cho, S. Rauf, V. Todorow, K. Ramaswamy, K. Collins, P. Stout, J. Y. Lee, J. Yoon, K. Shin, S. J. Choi, H. S. Cho, H. J. Kim, C. Lee, and D. Lymberopoulos, *Trans. Plasma Sci.* **37**, 1730 (2009).
- ¹⁸A. Agarwal, P. J. Stout, S. Banna, S. Rauf, K. Tokashiki, J.-Y. Lee, and K. Collins, *J. Appl. Phys.* **106**, 103305 (2009).
- ¹⁹P. Brichon, E. Despiau-Pujo, O. Mourey, and O. Joubert, *J. Appl. Phys.* **118**, 053303 (2015).
- ²⁰C. Larriba-Andaluz and S. L. Girshick, *Plasma Chem. Plasma Process.* **37**, 43 (2017).
- ²¹W. Chen, J.-L. Maurice, J.-C. Vanel, and P. Roca i Cabarrocas, *J. Phys. D: Appl. Phys.* **51**, 235203 (2018).
- ²²Th. Nguyen-Tran, P. Roca i Cabarrocas, and G. Patriarche, *Appl. Phys. Lett.* **91**, 11501 (2007).
- ²³N. Kodama, Y. Tanaka, K. Kita, Y. Uesugi, T. Ishijima, S. Watanabe, and K. Nakamura, *J. Phys. D: Appl. Phys.* **47**, 195304 (2014).
- ²⁴K. Akashi, Y. Tanaka, Y. Nakano, R. Furukawa, T. Ishijima, S. Sueyasu, S. Watanabe, and K. Nakamura, *Plasma Chem. Plasma Process.* **41**, 1121 (2021).
- ²⁵M. Kambara, S. Hamazaki, N. Kodama, and Y. Tanaka, *J. Phys. D: Appl. Phys.* **52**, 325502 (2019).
- ²⁶T. E. Sheridan and J. C. Gallagher, *Phys. Plasmas* **23**, 110703 (2016).
- ²⁷I. V. Schweigert and A. L. Alexandrov, *J. Phys. D: Appl. Phys.* **45**, 325201 (2012).
- ²⁸L. Wörner, A. V. Ivlev, L. Couédel, P. Huber, M. Schwabe, T. Hagl, M. Mikikian, L. Boufendi, A. Skvortsov, A. M. Lipaev, V. I. Molotkov,

- O. F. Petrov, V. E. Fortov, H. M. Thomas, and G. E. Morfill, *Phys. Plasmas* **20**, 123702 (2013).
- ²⁹I. B. Denysenko, N. A. Azarenkov, K. Ostrikov, and M. Y. Yu, *Phys. Plasmas* **25**, 013703 (2018).
- ³⁰B. van Minderhout, T. Peijnenburg, P. Blom, J. M. Vogels, G. M. W. Kroesen, and J. Beckers, *J. Phys. D: Appl. Phys.* **52**, 32LT03 (2019).
- ³¹B. van Minderhout, J. C. A. van Huijstee, B. Platier, T. Peijnenburg, P. Blom, G. M. W. Kroesen, and J. Beckers, *Plasma Sources Sci. Technol.* **29**, 065005 (2020).
- ³²N. Chaubey, J. Goree, S. J. Lanham, and M. J. Kushner, *Phys. Plasmas* **28**, 103702 (2021).
- ³³M. Mamunuru, R. Le Picard, Y. Sakiyama, and S. L. Girshick, *Plasma Chem. Plasma Process.* **37**, 701 (2017).
- ³⁴S. L. Girshick, *J. Vac. Sci. Technol. A* **38**, 011001 (2020).
- ³⁵S. N. Abolmasov, L. Kroely, and P. Roca i Cabarrocas, *Plasma Sources Sci. Technol.* **18**, 015005 (2009).
- ³⁶Z. Xiong, S. Lanham, E. Husmann, G. Nelson, M. A. Eslamisaray, J. Polito, Y. Liu, J. Goree, E. Thimsen, M. J. Kushner, and U. R. Kortshagen, *J. Phys. D: Appl. Phys.* **55**, 235202 (2022).
- ³⁷M. J. Kushner, *J. Phys. D: Appl. Phys.* **42**, 194013 (2009).
- ³⁸S. J. Lanham, J. Polito, X. Shi, P. Elvati, A. Violi, and M. J. Kushner, *J. Appl. Phys.* **130**, 163302 (2021).
- ³⁹M. J. Kushner, *J. Appl. Phys.* **71**, 4173 (1992).
- ⁴⁰J. Perrin, O. Leroy, and M. C. Bordage, *Contrib. Plasma Phys.* **36**, 3 (1996).
- ⁴¹R. Le Picard, A. H. Markosyan, D. H. Porter, S. L. Girshick, and M. J. Kushner, *Plasma Chem. Plasma Process.* **36**, 941 (2016).
- ⁴²M. Jiménez-Redondo, M. Cueto, J. L. Doménech, I. Tanarro, and V. J. Herrero, *RSC Adv.* **4**, 62030 (2014).
- ⁴³T. Zhang, J.-M. Orlac'h, M. Ghosh, V. Giovangigli, P. Roca i Cabarrocas, and T. Novikova, *Plasma Sources Sci. Technol.* **30**, 075024 (2021).
- ⁴⁴J. E. Allen, *Phys. Scr.* **45**, 497 (1992).
- ⁴⁵J. E. Allen, B. M. Annaratone, and U. De Angelis, *J. Plasma Phys.* **63**, 299 (2000).
- ⁴⁶C. Cui and J. Goree, *IEEE Trans. Plasma Sci.* **22**, 151 (1994).
- ⁴⁷J. E. Daugherty, R. K. Porteous, and D. B. Graves, *J. Appl. Phys.* **73**, 1617 (1993).
- ⁴⁸V. Vyas, G. A. Hebner, and M. J. Kushner, *J. Appl. Phys.* **92**, 6451 (2002).
- ⁴⁹M. D. Kilgore, J. E. Daugherty, R. K. Porteous, and D. B. Graves, *J. Appl. Phys.* **73**, 7195 (1993).
- ⁵⁰S. A. Khrapak, A. V. Ivlev, G. E. Morfill, and H. M. Thomas, *Phys. Rev. E* **66**, 046414 (2002).
- ⁵¹S. J. Choi and M. J. Kushner, *IEEE Trans. Plasma Sci.* **22**, 138 (1994).
- ⁵²L. Talbot, R. K. Cheng, R. W. Schefer, and D. R. Willis, *J. Fluid Mech.* **101**, 737 (1980).
- ⁵³G. K. Batchelor and C. Shen, *J. Colloid Interface Sci.* **107**, 21 (1985).
- ⁵⁴D. J. Rader and A. S. Geller, *Plasma Sources Sci. Technol.* **3**, 426 (1994).
- ⁵⁵X. Shi, P. Elvati, and A. Violi, *J. Phys. D: Appl. Phys.* **54**, 365203 (2021).
- ⁵⁶K. I. Hunter, J. T. Held, K. A. Mkhoyan, and U. R. Kortshagen, *ACS Appl. Mater. Interfaces* **9**, 8263 (2017).
- ⁵⁷A. Bapat, C. R. Perrey, S. A. Campbell, C. Barry Carter, and U. Kortshagen, *J. Appl. Phys.* **94**, 1969 (2003).
- ⁵⁸C. A. Beaudette, H. P. Andaraarachchi, C.-C. Wu, and U. R. Kortshagen, *Nanotechnology* **32**, 395601 (2021).
- ⁵⁹G. A. Hebner and C. B. Fleddermann, *J. Appl. Phys.* **82**, 2814 (1997).